Journal of Power Sources 203 (2012) 97–102

Contents lists available at SciVerse ScienceDirect

Journal of Power Sources

journal homepage: www.elsevier.com/locate/jpowsour

Synthesis of open tunnel-structured TiO_2(B) by nanosheets processes and its electrode properties for Li-ion secondary batteries

Hwamyung Jang[a,*], Shinya Suzuki[a], Masaru Miyayama[a,b]

[a] RCAST, University of Tokyo, Tokyo 153-8904, Japan
[b] JST, CREST, Tokyo 102-0075, Japan

ARTICLE INFO

Article history:
Received 20 July 2011
Received in revised form
28 November 2011
Accepted 29 November 2011
Available online 8 December 2011

Keywords:
Nanosheets processes
TiO_2(B)
Li-ion secondary batteries

ABSTRACT

Open tunnel-structured TiO_2(B) was synthesized by using nanosheets processes. TiO_2(B) was obtained only when multi-lamellar tetratitanate nanosheets were used as the reassembly component. The electrochemical properties of the nanosheet-derived TiO_2(B) were influenced by guest ions of the self-reassembled nanosheets. When K^+ ions were used as guest ions for the self-reassembly of nanosheets, the pure TiO_2(B) phase was obtained and it exhibited a large discharge capacity of 253 mAh(g-TiO_2(B))$^{-1}$ (x = 0.76, Li_xTiO_2(B)) at a current density of 100 mA(g-TiO_2(B))$^{-1}$. This value was a larger than 170 mA(g-TiO_2(B))$^{-1}$ of TiO_2(B) prepared by a conventional method without the nanosheets process. The large capacity is attributed to an increased specific surface area achieved by the nanosheets process.

1. Introduction

There are increasing demands of large-capacity and high-power energy storage devices for electric vehicles and various power tools. The Li-ion secondary battery is accepted as one of the best promising energy storage devices for those applications because of its high energy density. However, Li-ion secondary batteries still have several problems such as a low power density, high material cost, and safety problems [1,2]. Most of properties of Li-ion secondary batteries are determined by choosing adequate electrode materials and controlling microstructure of electrodes [1–3]. Thus, for choosing electrode materials, a large reversible capacity, high rate capability, and to be environmentally abundant and safe material are the important factors. TiO_2(B) has open tunnel structure in which Li^+ insertion reaction is fast [4,5], and a relatively large capacity around 200 mAh g^{-1} and good cyclic performance are reported [6–9]. The safety in overcharging is also improved by using TiO_2(B) as an anode material because its redox potential is relatively high as 1.6 V (vs. Li/Li^+) [6]. Thus, TiO_2(B) is accepted as one of the promising anode materials for Li-ion secondary batteries [4–9].

TiO_2(B) is one of metastable phases of TiO_2 and can be prepared by heat treatment of proton-exchanged layered titanate structure $A_2Ti_nO_{2n+1}$ (A = K, Na, Cs; n: $3 < n < 6$) [10–12]. The detailed phase transformation processes from those layered titanate structure to TiO_2(B) are not yet made clear, but it is known to have several transition steps which involve condensation of the interlayer hydroxyl groups and dehydration processes [13–15].

Recently, various nanostructured TiO_2(B) materials such as nanowires and nanotubes were synthesized and their electrode properties for Li-ion secondary batteries were reported [6–9]. Nanowire form of TiO_2(B) exhibited a large discharge capacity of 305 mAh(g-TiO_2(B))$^{-1}$ at a current density of 10 mA(g-TiO_2(B))$^{-1}$ and maintained a relatively large discharge capacity of 100 mAh(g-TiO_2(B))$^{-1}$ at a high current density of 2000 mA(g-TiO_2(B))$^{-1}$ [7]. Oriented TiO_2(B) films were also synthesized by electrophoretic deposition of exfoliated nanosheets suspension. However, its electrochemical properties were not studied yet [15].

Nanosheets are two-dimensional nanoparticles and can be prepared by exfoliation of layered structure. Nanosheets have extremely small thickness under 10 nm [16]. Prepared nanosheets from metal oxide compounds are usually charged negatively and dispersed in various solutions. Self-reassembly of nanosheets occurs by reaction with cations such as protons from acid solutions, alkaline metal ions, and alkaline earth metal ions [18,22]. Synthesis of electrode materials using nanosheets processes is advantageous for enhancing electrode properties, since microstructural control of electrode materials and homogeneous mixing with conducting materials can be achieved easily during the self-assembling process.

Our group has reported the synthesis processes using nanosheets and electrode properties of several titanate hydrate compounds like layer-structured $H_2Ti_4O_9 \cdot nH_2O$ and tunnel-structured $H_2Ti_8O_{17} \cdot nH_2O$ [17–19]. Those layer- and tunnel-structured titanate hydrate compounds have some crystal water

* Corresponding author. Tel.: +81 3 5452 5082; fax: +81 3 5452 5083.
E-mail address: janghwamyung@crm.rcast.u-tokyo.ac.jp (H. Jang).

0378-7753/$ – see front matter © 2011 Elsevier B.V. All rights reserved.
doi:10.1016/j.jpowsour.2011.11.078

which limits the reversible capacity and rate capability. In the case of TiO_2(B), a large reversible capacity and good rate capability are expected since there are no crystal water in the tunnel structure. However, the detailed synthesis process of TiO_2(B) from tetratitanate nanosheets is not fully understood and its effects of microstructure on electrode properties have not yet reported.

In this work, the synthesis of open tunnel-structured TiO_2(B) was conducted by using tetratitanate nanosheets and its electrode properties for Li-ion secondary batteries were examined. The detailed phase transformation process of TiO_2(B) from nanosheets were also discussed.

2. Experimental

$K_2Ti_4O_9$ was prepared by a conventional method using solid-state reaction [12]. K_2CO_3 and TiO_2 (rutile) were mixed in the molar ratio 1:3.95 and heated at 800 °C for 20 h. The sintered powders were ground and heated at 800 °C for another 20 h. Proton-exchange on K^+ ions was carried out by stirring $K_2Ti_4O_9$ with HCl aqueous solution for 0.5 h. The molar ratio of HCl solution to $K_2Ti_4O_9$ was 1:2. Exfoliation of proton-exchanged $H_{1.93}K_{0.07}Ti_4O_9{\cdot}nH_2O$ occurred by reaction with large organic ions [15]. Prepared proton-exchanged $H_{1.93}K_{0.07}Ti_4O_9{\cdot}nH_2O$ powder was reacted with 200 cm^3 of aqueous solution of ethylamine for 24 h. The obtained ethylammonium-intercalation compound (EA-$H_{1.93}K_{0.07}Ti_4O_9{\cdot}nH_2O$) was reacted with 200 cm^3 of aqueous solution of tetrabutylammonium hydroxide for 48 h. 10-fold molar ratio of ethylamine and tetrabutylammonium hydroxide to $H_{1.93}K_{0.07}Ti_4O_9{\cdot}nH_2O$ were used for these reactions. A colloidal suspension of tetratitanate nanosheets was prepared by dispersing the tetrabutylammonium-intercalation compound (TBA-$H_{1.93}K_{0.07}Ti_4O_9{\cdot}nH_2O$) in distilled water. Nanosheets were separated from the obtained colloidal suspension using centrifugal separation at various rpm. Separated nanosheets were self-reassembled by adding 0.3 mol dm^{-3} HCl into the colloidal suspension. Self-reassembled nanosheets ($H_{1.99}K_{0.01}Ti_4O_9{\cdot}nH_2O$) were obtained as precipitates. Obtained precipitates were washed with distilled water, dried at 80 °C for 2 h, and subsequently heat-treated at 400 °C for 1 h to convert to TiO_2(B).

The exfoliated nanosheets were also self-reassembled by using K^+ ions instead of H^+ ions. The K^+ ions of the self-reassembled nanosheets ($H_{1.36}K_{0.64}Ti_4O_9{\cdot}nH_2O$) were exchanged into H^+ ions ($H_{1.96}K_{0.04}Ti_4O_9{\cdot}nH_2O$), and subsequently heat-treated at 350 °C for 1 h to convert to TiO_2(B). Conventional powder form of TiO_2(B) was synthesized by heat treatment of $H_{1.93}K_{0.07}Ti_4O_9{\cdot}nH_2O$ for comparison.

The crystal structure of samples was confirmed by X-ray diffraction (XRD) analysis using an X-ray diffractometer D8 ADVANCE (BRUKER). The morphologies of the tetratitanate nanosheets and heat-treated samples were observed by atomic force microscopy (AFM), SPI3800 (SEIKO INSTRUMENTS), and scanning electron microscopy (SEM), S-4500 (HITACHI). The specific surface area and pore size distribution of samples were determined by a gas absorption method using TriStar 3000 (MICRO MERITICS). The composition and the amount of hydrated water in samples were determined by the inductively coupled plasma (ICP) spectroscopy, SPS3100 (SEIKO INSTRUMENTS), and the thermal gravimetry (TG), TG8120 (RIGAKU).

Working electrodes for electrochemical measurements were fabricated by pressing a mixture of obtained TiO_2(B) and acetylene black (AB) and polytetrafluoroethylene (PTFE) with a weight ratio of 45:45:10 onto a Ni mesh at a pressure of ~150 MPa. The TiO_2(B) loading in the working electrodes was fixed to be 15 mg cm^{-2}. Electrochemical measurements were performed using a three electrode cell with lithium strips as the reference electrode and the counter electrode, and prepared TiO_2(B) electrode as the working electrode. A 1 mol dm^{-3} lithium perchlorate in propylene carbonate (KISHIDA CHEMISTRY) was used as an electrolyte. Galvanostatic discharge/charge tests and cyclic voltammetry (CV) test were carried out in the voltage range from 1.2 to 3.6 V (vs. Li^+/Li) using 1470E CELLTEST SYSTEM (SOLARTRON) and HZ-3000 (HOKUTO DENKO).

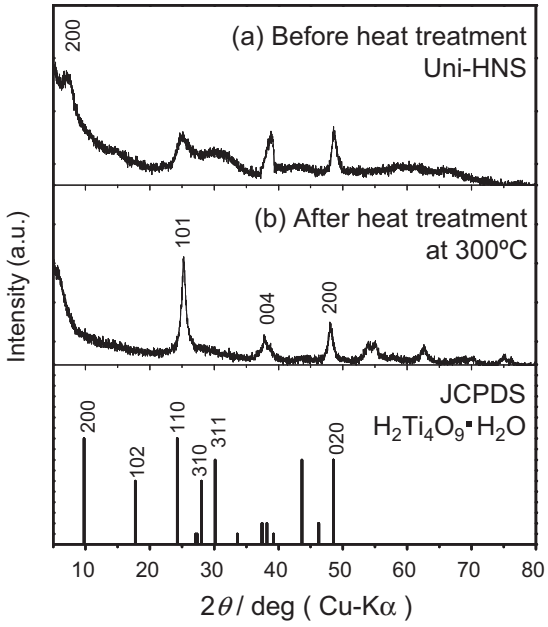

Fig. 1. XRD patterns for Uni-HNS (a) before heat treatment, (b) after heat treatment at 300 °C, and JCPDS data for $H_2Ti_4O_9{\cdot}H_2O$.

3. Results and discussion

Prepared tetratitanate nanosheets which were separated centrifugally at 15,000 rpm had 1 nm in thickness. This thickness corresponds to a single or two oxide layers [16]. Obtained uni-lamellar nanosheets were self-reassembled by using H^+ ions and heat treated to convert to TiO_2(B). Fig. 1 shows XRD patterns for before and after heat treatments of self-reassembled uni-lamellar nanosheets (Uni-HNS) at 300 °C. Before the heat treatment, Uni-HNS showed broad several peaks and the 2 0 0 peak, the basal peak of layered structure, was largely shifted to a low angle (Fig. 1a). After the heat treatment at 300 °C, the anatase phase of TiO_2 was observed instead of TiO_2(B) (Fig. 1b). The anatase phase, one of metastable phases of TiO_2, is usually formed by heating layer-structured $H_2Ti_4O_9{\cdot}nH_2O$ around 800 °C. However, the anatase phase appeared at much lower temperature around 300 °C in the present process. These results indicate that uni-lamellar tetratitanate nanosheets exhibit different phase transformation processes compared to conventional powders of layer-structured $H_2Ti_4O_9{\cdot}nH_2O$.

Synthesis of TiO_2(B) was also attempted by using multi-lamellar nanosheets. After the reaction with TBAOH aqueous solution, layer-structured tetratitanate exfoliated into various nanosheets with different thicknesses. To separate thick nanosheets, multi-lamellar nanosheets, nanosheets were centrifugally separated at several steps. The first, uni-lamellar nanosheets were removed at 15,000 rpm as a supernatant. The second, obtained precipitation was dispersed in distilled water and multi-lamellar nanosheets were centrifugally separated at 1500 rpm as a supernatant. Fig. 2 shows atomic force microscopy images of prepared nanosheets. Obtained nanosheets had a plate-like morphology, 200 nm in

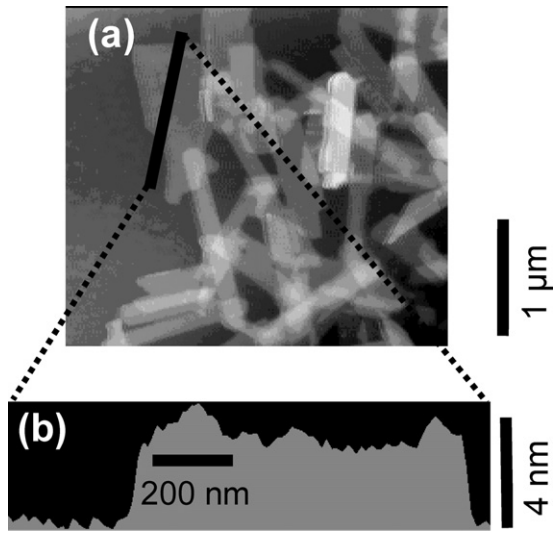

Fig. 2. (a) AFM image of prepared multi-lamellar nanosheets at 1500 rpm and (b) cross-sectional analysis of the indicated line in (a).

width, 1 μm in length, and 4 nm in thickness. According to its thickness, multi-lamellar nanosheets consist of approximately 5 oxide layers [16]. Obtained multi-lamellar nanosheets were self-reassembled by using H^+ ions and heat-treated to convert to TiO_2(B). Fig. 3 shows XRD patterns of self-reassembled multi-lamellar tetratitanate nanosheets (Mul-HNS) for (a) before heat treatment, (b) after heat treatment at 200 °C, and (c) at 400 °C. Before the heat treatment, Mul-HNS showed good agreement with peaks of layer-structured $H_2Ti_4O_9{\cdot}nH_2O$ (Fig. 3a). After the heat treatment at 200 °C, peaks of $H_2Ti_8O_{17}{\cdot}nH_2O$ were observed (Fig. 3b). After the heat treatment at 400 °C, peaks of TiO_2(B) were observed, though they were a little broad (Fig. 3c). Thus, nanosheet-derived TiO_2(B) (NS-TiO_2(B))was successfully synthesized from Mul-HNS.

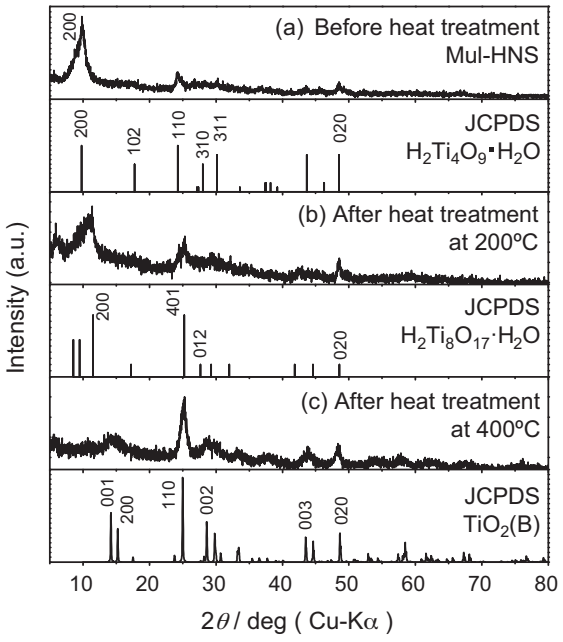

Fig. 3. XRD patterns of Mul-HNS for (a) before heat treatment, (b) after heat treatment at 200 °C, and (c) at 400 °C, respectively, with JCPDS data for $H_2Ti_4O_9{\cdot}H_2O$, $H_2Ti_8O_{17}{\cdot}H_2O$, and TiO_2(B).

The nanosheet-derived TiO_2(B) was also obtained when K^+ ions were used as guest ions for the self-reassembly of multi-lamellar nanosheets. K^+ ions of the self-reassembled nanosheets were exchanged into H^+ ions (Mul-KNS) and heat-treated to convert to TiO_2(B) phase (KNS-TiO_2(B)). KNS-TiO_2(B) had sharp peaks and showed good agreements with the JCPDS data of TiO_2(B). The peaks of the anatase phase of TiO_2 were not observed.

Conventional powders of $H_2Ti_4O_9{\cdot}nH_2O$ are known to transform to TiO_2(B) at 350 °C through an intermediate phase $H_2Ti_8O_{17}{\cdot}nH_2O$ [12,21]. $H_2Ti_8O_{17}{\cdot}nH_2O$ is an intermediate phase and can be prepared from conventional $H_2Ti_4O_9{\cdot}nH_2O$ powders and multi-lamellar tetratitanate nanosheets by heat treatment at 300 °C and 200 °C, respectively [18,19,21]. During the phase transformation process to TiO_2(B), condensation of interlayer hydroxyl groups and dehydration processes occur in interlayer space of layer-structured $H_2Ti_4O_9{\cdot}nH_2O$ [13–15].

Fig. 4 shows schematic images of phase transformation process from the self-reassembled multi-lamellar nanosheets to TiO_2(B). This process is observed when multi-lamellar nanosheets were self-reassembled by H^+ or K^+ ions. However, when uni-lamellar nanosheets were used, TiO_2(B) and any intermediate phases were not observed by heat treatments (Fig. 1). The interlayer space of Uni-HNS, Mul-HNS, and Mul-KNS were calculated with the 200 peak, the basal peak of layered structure, using the following equation [15,20].

$$d_{\text{interlayer}} = d_{(200)} \times \sin\alpha - d_{\text{oxide sheet}}$$

The values $d_{\text{oxide sheet}} = 0.56$ nm and $\alpha = 104^\circ$ were used in this equation [20]. The interlayer space of conventional powders of $H_{1.93}K_{0.07}Ti_4O_9{\cdot}nH_2O$ is around 0.27 nm. The interlayer space of Uni-HNS, Mul-HNS, and Mul-KNS was estimated to be approximately 0.59 nm, 0.31 nm, and 0.27 nm, respectively. Mul-HNS and Mul-KNS had the almost same interlayer space with conventional powders of $H_{1.93}K_{0.07}Ti_4O_9{\cdot}nH_2O$. This would be a reason for that TiO_2(B) was obtained from the self-reassembled multi-lamellar nanosheets but not from the self-reassembled uni-lamellar nanosheets. Thus, This result indicates that interlayer space is an important factor to synthesis of TiO_2(B) from tetratitanate nanosheets.

Fig. 5 shows SEM images for (a) Mul-HNS and (b) NS-TiO_2(B). Before the heat treatment, Mul-HNS particles were in large agglomeration of nanosheets over 10 μm (Fig. 5a). On the particle, plate-like morphology of nanosheets was observed. After the heat treatment at 400 °C, NS-TiO_2(B) particles maintained its plate-like morphology (Fig. 5b). It suggests that the nanosheets process is a useful method to achieve microstructure-controlled TiO_2(B) electrode materials because tetratitanate nanosheets keep its morphology after TiO_2(B) phase transformation. When K^+ ions were used, Mul-KNS and KNS-TiO_2(B) had similar morphologies to Mul-HNS and NS-TiO_2(B). Mul-KNS also showed a large particle size over 10 μm. The large agglomeration of KNS-TiO_2(B) and NS-TiO_2(B) is probably caused by the self-assembly process of nanosheets, in which negatively charged nanosheets keep on self-reassembling during cations, H^+ or K^+ ions, are supplied.

Fig. 6 shows cyclic voltammograms (CV) curves for (a) KNS-TiO_2(B), (b) NS-TiO_2(B), and (c) the conventional powder form of TiO_2(B) (Bulk-TiO_2(B)) at a scan rate of 0.1 mA s^{-1}. Bulk-TiO_2(B) exhibited two pairs of cathodic and anodic current peaks at around 1.5 V and 1.6 V, which are characteristic for Li-insertion/deinsertion of TiO_2(B) phase, respectively [4]. NS-TiO_2(B) exhibited also two pairs of cathodic and anodic current peaks at 1.5 V and 1.6 V, respectively. Those current peaks were weak and broad compared to Bulk-TiO_2(B). In addition, NS-TiO_2(B) showed another pair of cathodic and anodic current peaks at 1.75 V and 2.0 V, which is characteristic for Li-insertion/deinsertion of the anatase phase of

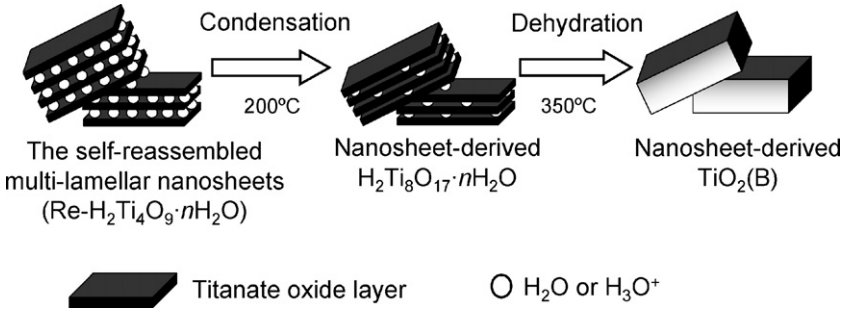

Fig. 4. Schematic images of TiO_2(B) phase transformation process from the self-reassembled multi-lamellar nanosheets.

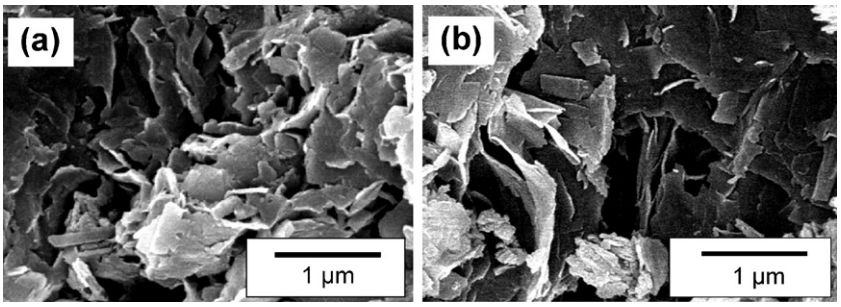

Fig. 5. SEM images for (a) Mul-HNS and (b) NS-TiO_2(B).

TiO_2, respectively [4]. In the other hand, KNS-TiO_2(B) exhibited only cathodic and anodic current peaks at around 1.5 V and 1.6 V which are characteristic for Li-insertion/deinsertion of TiO_2(B) phase, respectively [4]. Cathodic and anodic current peaks for the anatase phase of TiO_2 were not observed. These results indicate that TiO_2(B) phase is only electrochemically active phase in KNS-TiO_2(B) and Bulk-TiO_2(B). However, little amount of the anatase phase of TiO_2 existed in NS-TiO_2(B). According to the amount of current peaks at 1.75 V and 2.0 V, approximately 10–20% of capacity for NS-TiO_2(B) was caused by Li-insertion/deinsertion at the anatase phase.

Fig. 7 shows the 10th discharge curves for (a) KNS-TiO_2(B), (b) NS-TiO_2(B), and (c) Bulk-TiO_2(B) at a current density of 100 mA(g-TiO_2(B))$^{-1}$ and 1000 mA(g-TiO_2(B))$^{-1}$. At a current density of 100 mA(g-TiO_2(B))$^{-1}$, KNS-TiO_2(B) showed increased working potential and exhibited a large discharge capacity of 253 mAh(g-TiO_2(B))$^{-1}$ (x = 0.76, Li_xTiO_2(B)). NS-TiO_2(B) also exhibited a large discharge capacity of 190 mAh(g-TiO_2(B))$^{-1}$ (x = 0.56,

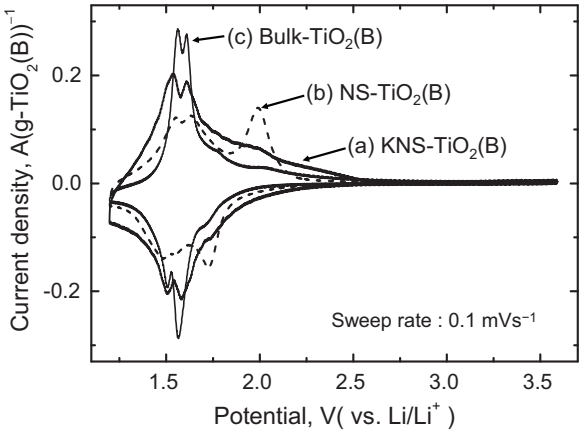

Fig. 6. CV curves for (a) KNS-TiO_2(B), (b) NS-TiO_2(B), and (c) Bulk-TiO_2(B) at 0.1 mV s^{-1}.

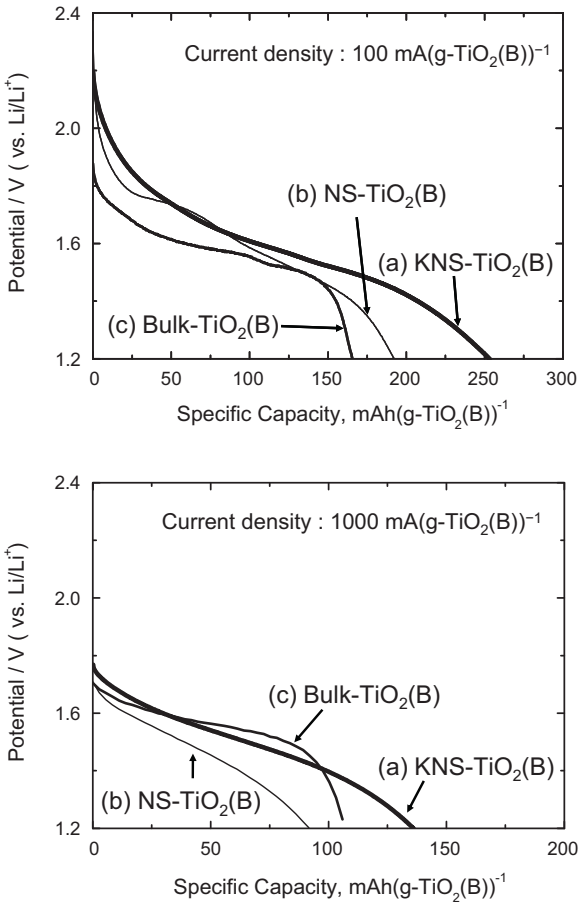

Fig. 7. The 10th discharge curves for (a) KNS-TiO_2(B), (b) NS-TiO_2(B), and (c) Bulk-TiO_2(B) at a current density of 100 mA(g-TiO_2(B))$^{-1}$ and 1000 mA(g-TiO_2(B))$^{-1}$.

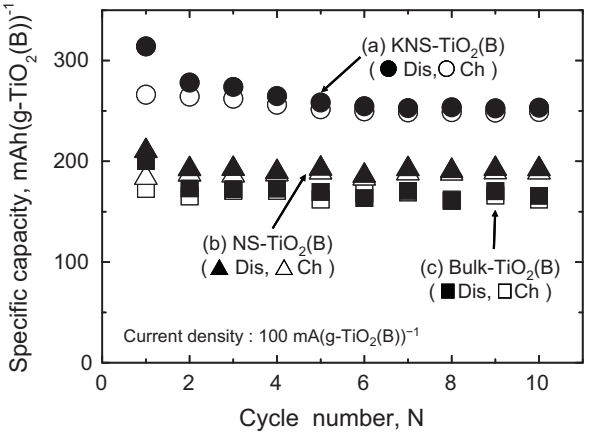

Fig. 8. A cyclic performance for (a) KNS-TiO_2(B), (b) NS-TiO_2(B), and (c) Bulk-TiO_2(B) at a current density of 100 mA(g-TiO_2(B))$^{-1}$.

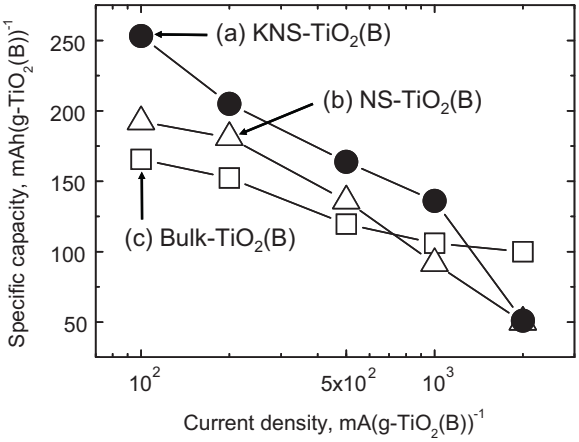

Fig. 9. Rate capability for (a) KNS-TiO_2(B), (b) NS-TiO_2(B), and (c) Bulk-TiO_2(B) at various current densities.

Li_xTiO_2(B)) than 170 mAh(g-TiO_2(B))$^{-1}$ of Bulk-TiO_2(B). At a high current density of 1000 mA(g-TiO_2(B))$^{-1}$, KNS-TiO_2(B) and Bulk-TiO_2(B) maintained a relatively large discharge capacity of 136 mAh(g-TiO_2(B))$^{-1}$ and 106 mAh(g-TiO_2(B))$^{-1}$, respectively. However, NS-TiO_2(B) showed a large IR drop and a small discharge capacity of 91 mAh(g-TiO_2(B))$^{-1}$.

We have reported that the nanosheet-derived $H_2Ti_8O_{17}{\cdot}nH_2O$ electrode material exhibited a larger reversible capacity and smaller overvoltage than conventional powders of $H_2Ti_8O_{17}{\cdot}nH_2O$ because the interfacial kinetic resistance of the electrode decreases with an increase in surface area [18].

Since KNS-TiO_2(B) and NS-TiO_2(B) had a large specific surface area of 66 $m^2\,g^{-1}$ and 77 $m^2\,g^{-1}$ compared to 11 $m^2\,g^{-1}$ of Bulk-TiO_2(B), those nanosheet-derived TiO_2(B) showed a larger discharge capacity at a current density of 100 mA(g-TiO_2(B))$^{-1}$. At a high current density of 1000 mA(g-TiO_2(B))$^{-1}$, NS-TiO_2(B) showed a large IR drop and low rate capability compared to KNS-TiO_2(B). The second phase in NS-TiO_2(B) could be a reason for poor electrochemical properties. NS-TiO_2(B) had the anatase TiO_2 phase as a second phase. The anatase phase of TiO_2 also works as a host material for Li^+ insertion/deinsertion [4]. However, the anatase phase of TiO_2 has no fast Li^+ ion diffusion paths such as the tunnel structure of the TiO_2(B) phase. Since the anatase phase exists in NS-TiO_2(B), fast Li^+ ion diffusion paths become disorder and smooth connection of tunnel to tunnel is interfered. Thus, the Li-ion diffusion become slow, leading to low rate capability of NS-TiO_2(B).

Fig. 8 shows a cyclic performance for (a) KNS-TiO_2(B), (b) NS-TiO_2(B), and (c) Bulk-TiO_2(B) at a current density of 100 mA(g-TiO_2(B))$^{-1}$. Those three TiO_2(B) electrodes showed a good cyclic performance. KNS-TiO_2(B) exhibited a large discharge capacity of 258 mAh(g-TiO_2(B))$^{-1}$ at the 5th cycle and maintained a large discharge capacity of 253 mAh(g-TiO_2(B))$^{-1}$ after 10 cycles.

Fig. 9 shows rate capability for (a) KNS-TiO_2(B), (b) NS-TiO_2(B), and (c) Bulk-TiO_2(B) at various current densities. KNS-TiO_2(B) and NS-TiO_2(B) showed a larger discharge capacity compared to Bulk-TiO_2(B) at a wide range of current densities. However, a discharge capacity of KNS-TiO_2(B) and NS-TiO_2(B) decreased to 50 mAh(g-TiO_2(B))$^{-1}$ at a high current density of 2000 mA(g-TiO_2(B))$^{-1}$. In the other hand, Bulk-TiO_2(B) maintained a relatively large discharge capacity of 100 mAh(g-TiO_2(B))$^{-1}$. According to SEM measurements, KNS-TiO_2(B) and NS-TiO_2(B) had a large particle size over 10 μm. This was almost 10 times as large as Bulk-TiO_2(B), which has a plate-like morphology, ~1 μm in length, ~200 nm in width, and 200–300 nm in thickness. Accordingly, in KNS-TiO_2(B) and NS-TiO_2(B), it is difficult to achieve a large contact area between nanosheet-derived TiO_2(B) particles and electronically conductive carbon particles, even though KNS-TiO_2(B) and NS-TiO_2(B) contain a large amount of carbon of 45 wt%. Thus, the inside of these nanosheet-derived TiO_2(B) particles has low electronic conductivity, leading to low rate capability.

The pure phase of TiO_2(B), KNS-TiO_2(B), was successfully synthesized and KNS-TiO_2(B) showed improved electrochemical properties compared to NS-TiO_2(B). Sugimoto et al. reported that the presence of organic compounds in interlayer of nanosheets seems to inhibit the transformation to tunnel-structured TiO_2(B) and promote the generation of the anatase phase of TiO_2 [15]. When uni-lamellar nanosheets were used, Uni-HNS had an extended interlayer space and the anatase phase of TiO_2 was generated. Those structural defects or distortions on the nanosheets could be the reasons for the generation of the anatase phase of TiO_2. The K^+ ion is the original guest ion of the exfoliated nanosheets. Since the original guest ion, the K^+ ion, was used for the self-reassembly of exfoliated nanosheets, structural defects or distortions were inhibited and the pure TiO_2(B) phase was generated in KNS-TiO_2(B). Further studies for the effects of guest ions are under investigation. Since KNS-TiO_2(B) had large particle size over 10 μm, better rate capability can be achieved by reducing its particle size and making composites with conducting materials such as graphene or carbon nanotube.

4. Conclusions

The powder form of nanosheet-derived TiO_2(B) was successfully synthesized and its electrode properties were measured at the first time. TiO_2(B) was only obtained when the self-reassembled multi-lamellar tetratitanate nanosheets were used as the reassembly component. These results indicates that the interlayer structure of tetratitanate nanosheets is important factor to synthesis of open tunnel-structured TiO_2(B).

The electrochemical properties of the nanosheet-derived TiO_2(B) were influenced by guest ions of self-reassembled nanosheets. When K^+ ions were used as guest ions, pure TiO_2(B) phase was obtained and KNS-TiO_2(B) showed improved electrochemical properties.

KNS-TiO_2(B) exhibited a large discharge capacity of 258 mAh(g-TiO_2(B))$^{-1}$ (x = 0.77, Li_xTiO_2(B)) at the 5th cycle and maintained a large capacity of 253 mAh(g-TiO_2(B))$^{-1}$ (x = 0.76, Li_xTiO_2(B)) after 10 cycles at a current density of 100 mA(g-TiO_2(B))$^{-1}$. At a high current density of 1000 mA(g-TiO_2(B))$^{-1}$, KNS-TiO_2(B) maintained a relatively large discharge capacity of 136 mAh(g-TiO_2(B))$^{-1}$. Since KNS-TiO_2(B) had a large particle size over 10 μm, better rate

capability can be achieved by reducing its particle size and making composites with conducting materials.

References

[1] R. Kanno, G.S. Yuasa, Tech. Rep. 3 (2006) 1–11.
[2] J.P. Peres, F. Perton, C. Audry, P. Biensan, A. Guibert, G. Blanc, M. Broussely, J. Power Sources 97–98 (2001) 702–710.
[3] J.M. Tarascon, M. Armand, Nature 414 (2001) 359–367.
[4] M. Zukalova, M. Kalbac, L. Kavan, I. Exnar, M. Graetzel, Chem. Mater. 17 (2005) 1248–1255.
[5] C. Arrouvel, S.C. Parker, M.S. Islam, Chem. Mater. 21 (2009) 4778–4783.
[6] G. Armstrong, A.R. Armstrong, J. Canales, P.G. Bruce, Electrochem. Solid State Lett. 9 (2006) A139–A143.
[7] A.R. Armstrong, G. Armstrong, J. Canales, P.G. Bruces, J. Power Sources 146 (2005) 501–506.
[8] A.R. Armstrong, G. Armstrong, J. Canales, P.G. Bruce, Angew. Chem. Int. Ed. 116 (2004) 2336–2338.
[9] L.P. An, X.P. Gao, G.R. Li, T.Y. Yan, H.Y. Zhu, P.W. Shen, Electrochim. Acta 53 (2008) 4573–4579.
[10] T.P. Feist, S.J. Mocarski, P.K. Davies, J. Solid State Ionics 28–30 (1988) 1338–1343.
[11] R. Marchand, L. Brohan, M. Tournoux, Mater. Res. Bull. 15 (1980) 1129–1133.
[12] T.P. Feist, P.K. Davies, J. Solid State Chem. 101 (1992) 275–295.
[13] E. Morgado Jr., P.M. Jardim, B.A. Marinkovic, F.C. Rizzo, M.A.S. Abreu, J.L. Zotin, A.S. Araujo, J. Nanotechnol. 18 (2007) 495710.
[14] M. Tournoux, R. Marchand, L. Brohan, J. Solid State Chem. 17 (1986) 33–52.
[15] W. Sugimoto, O. Terabayashi, Y. Murakami, Y. Takasu, J. Mater. Chem. 12 (2002) 3814–3818.
[16] N. Sakai, Y. Ebina, K. Takada, T. Sasaki, J. Am. Chem. Soc. 126 (2004) 5851–5858.
[17] S. Suzuki, M. Miyayama, Key Eng. Mater. 248 (2003) 151–154.
[18] S. Suzuki, M. Miyayama, J. Phys. Chem. B 110 (2006) 4731–4734.
[19] S. Suzuki, M. Miyayama, J. Electrochem. Soc. 154 (5) (2007) A438–A443.
[20] M. Yanagisawa, S. Uchida, S. Yin, T. Sato, Chem. Mater. 13 (2001) 174–178.
[21] H. Izawa, S. Kikkawa, M. Koizumi, J. Phys. Chem. 86 (1982) 5023–5026.
[22] Y. Ebina, T. Sasaki, M. Harada, M. Watanabe, Chem. Mater. 14 (2002) 4390–4395.